Computer-Based Modeling of Novel Carbon Systems and Their Properties

CARBON MATERIALS: CHEMISTRY AND PHYSICS

A comprehensive book series which encompasses the complete coverage of carbon materials and carbon-rich molecules from elemental carbon dust in the interstellar medium, to the most specialized industrial applications of the elemental carbon and derivatives. A great emphasis is placed on the most advanced and promising applications ranging from electronics to medicinal chemistry. The aim is to offer the reader a book series which not only consists of self-sufficient reference works, but one which stimulates further research and enthusiasm.

Series Editors

Dr. Prof. Franco Cataldo
Director of Lupi Chemical
Research Institute
Via Casilina 1626/A
00133 Rome
Italy

Professor Paolo Milani
University of Milan
Department of Physics
Via Celoria, 26
20133, Milan
Italy

VOLUME 3:
COMPUTER-BASED MODELING OF NOVEL CARBON SYSTEMS AND THEIR PROPERTIES: BEYOND NANOTUBES

Volume Editors

Prof. Luciano Colombo
Department of Physics
University of Cagliari
Cittadella Univeritaria
I-09042 Monserrato (Ca)
Italy

Prof. Annalisa Fasolino
Theory of Condensed Matter
Institute for Molecules and Materials
Radboud University Nijmegen
Heyendaalseweg 135
6525 AJ Nijmegen
The Netherlands

For other titles published in this series, go to
http://www.springer.com/series/7825

Luciano Colombo • Annalisa Fasolino
Editors

Computer-Based Modeling of Novel Carbon Systems and Their Properties

Beyond Nanotubes

Springer

Editors
Prof. Luciano Colombo
Department of Physics
University of Cagliari
Monserrato, Italy
luciano.colombo@dsf.unica.it

Prof. Annalisa Fasolino
Theory of Condensed Matter
Institute for Molecules and Materials
Radboud University Nijmegen, Nijmegen
The Netherlands
a.fasolino@science.ru.nl

ISSN 1875-0745 e-ISSN 1875-0737
ISBN 978-1-4020-9717-1 e-ISBN 978-1-4020-9718-8
DOI 10.1007/978-1-4020-9718-8
Springer Dordrecht New York Heidelberg London

Library of Congress Control Number: 2010929765

Preface

The number of observed or guessed atomic architectures formed by elemental carbon has unexpectedly increased in the last decades. In addition to graphite and diamond, a multiplicity of other structures – such as well ordered fullerenes and nanotubes, or less ordered structures like nanoporous and amorphous carbon – have been synthesized and studied. Similarly to what happens for diamond with respect to graphite, the new metastable phases (although basically sp^2-bonded) are definitely other than graphite (still to consider as the most stable phase) as for their physical and chemical features in a wide range of temperatures and pressures. Interestingly, the mechanical, structural, and electronic properties of these new forms of carbon are extremely different, ranging from soft to hard, from compact to open, from insulating to metallic.

Theory and simulations have largely contributed to understand and characterize the new carbon-based systems and led to the prediction of new ones. The multiplicity of possible arrangements, the diversity of behaviors, and the complex interplay between structures and properties poses a formidable challenge to theoretical and computational physicists. A number of different methods are therefore needed, ranging from model-potential molecular dynamics, to tight-binding calculations, to first-principles simulations. As a general feeling, it is also becoming evident that their combination into a unique theoretical and computational tool is actually needed to make new progress in this field.

This volume presents a unique survey of the theoretical modeling of all phases of carbon – other than single fullerene molecules or nanotubes – from natural crystalline forms found on earth and in meteorites to artificial (hypothetical) nanofoams. In addition, the present volume deals with the computational techniques used to understand and predict the structure and properties of such carbon systems, as well as reports about the present state of the art, including controversial aspects like the occurrence of magnetism, and presents open questions for the future. Although the main focus is on carbon-based systems, the computational challenges posed by their diverse structural, bonding, mechanical and electronic properties are relevant for all materials and make the present volume valuable for the whole community of computational condensed matter physics.

Each chapter is a self-contained authoritative exposition by scientists with an international reputation, sharing their knowledge and tricks of the trade. As a whole, the book provides a basis towards a unified theoretical description of carbon, the most fascinating element in Nature.

The first part of the volume is mostly devoted to the structural properties of several novel carbon structures.

Chapter 1 by Ghiringhelli and Meijer opens with a description of the phase diagram of carbon that includes its traditional phases, diamond, graphite and liquid carbon. Graphite and diamond melt into a liquid with a network-like microscopic structure at extremely high values of pressure and temperature. The phase diagram of carbon is experimentally poorly known and recent simulations give access to its determination.

The diamond structure can also become extremely stable at the nanoscale, as extensively discussed in Chapter 2 by Galli, where nanoparticles with diamond-like structures, formed in a wide variety of natural environments (around stars or in CVD phases) or under very high pressure and temperature conditions, are investigated.

Since the discovery of fullerenes and nanotubes, that are not treated in detail here, several other new forms of nanostructured carbon mostly based on the graphitic sp^2 bond configuration have been identified. Chapter 3 by Seifert, Kuc and Heine introduces the carbon nanofoams, hypothetical ordered graphitic structures that display interesting analogies with carbon nanotubes. Although not yet firmly established, these structures might have been possibly experimentally realized.

The second part of the volume is more focused on the physico-chemical properties of several exotic carbon architectures.

Chapter 4 by Carlsson introduces a more general type of structure based on sp^2 bonding called nanoporous carbon, a class of materials that have been obtained by a number of experimental methods. Nanoporous carbon and nanofoams promise to have specific cathalitic action and great potential for chemical applications.

Chapter 5 by Marks examines amorphous carbon, currently among the most interesting materials for applications. Computer simulations have largely contributed to the complex characterization of this disordered type of structure. The contribution provides a critical exam of the criteria for theory to be accurate enough to discern between different structural models.

Chapter 6 by Blase, Benedek and Bernasconi examines the exceptional mechanical properties of clathrate structures. The criteria for designing hard materials are examined, also in connection with electronic properties and possible occurrence of superconductivity.

Finally in Chapter 7 by Ganchenkova, Vehviläinen and Nieminen, the intriguing, but still controversial observation of ferromagnetism in nanostructured carbon, such as polymerised fullerenes and ion-irradiated graphitic materials is examined and the conditions for ferromagnetic ordering defect-related magnetism are explored.

Luciano Colombo
Annalisa Fasolino

Contents

Chapter 1
Liquid Carbon: Freezing Line and Structure Near Freezing

Luca M. Ghiringhelli[1] and Evert Jan Meijer[2]

Abstract This chapter deals with the phase diagram of carbon with emphasis on the liquid phase occurring in extreme conditions of temperature and pressure. After presenting a critical review of the experimental results and still unresolved issues, the authors discuss the possibility of modeling carbon by use of empirical potentials. Also the techniques to evaluate numerically the free energy of each phase are presented in detail. The second part of the chapter discusses in detail the structure of the liquid in different ranges of pressure, the pressure–density equations of state at different temperatures and the possibility of a liquid–liquid phase transition.

1.1 Introduction

Carbon exhibits a rich variety of solid structures such as the familiar crystalline graphite and diamond state, or amorphous states such as glassy carbon or carbon black. More recently additional (metastable) phases have been found or predicted. These include carbynes [1, 2] and M-carbon [3]. In addition to the bulk phases there are various other recently discovered structures including fullerenes [4], nanotubes [5], and graphene [6].

Knowledge of the phase diagram of carbon is of crucial importance for a better understanding of a wide variety of physical phenomena and properties of carbon-based materials. For example, the phase diagram determines the carbon content of the interior of the Earth and other planets and it determines the optimal conditions for the manufacturing of synthetic diamonds. Knowledge of the graphite melting line is relevant for the formation mechanism of low dimensional layered structures that are important in fundamental and technological applications.

[1]Fritz Haber Institute of the Max Planck Society, Faradayweg 4-6, D-14195, Berlin, Germany
e-mail: luca@fhi-berlin.mpg.de

[2]Van't Hoff Institute for Molecular Sciences & Amsterdam Center for Multiscale Modeling, Universiteit van Amsterdam, Nieuwe Achtergracht 166, NL-1018 WV, Amsterdam, The Netherlands
e-mail: e.j.meijer@uva.nl

L. Colombo and A. Fasolino (eds.), *Computer-Based Modeling of Novel Carbon Systems and Their Properties*, Carbon Materials: Chemistry and Physics 3,
DOI 10.1007/978-1-4020-9718-8_1,

The phase diagram of carbon has been intensively studied, both experimentally and by theoretical and numerical methods [1, 7–11, 11–26]. These studies covered pressures (P) and temperatures (T) ranging up to 100 GPa and 10,000 K. Until recently the knowledge of the carbon phase diagram was still fragmented because experiments under these conditions are difficult if not outright impossible, whereas quantitative theoretical and numerical predictions were hampered by the fact that the existing atomistic models for carbon had serious flaws that made them unsuited for quantitative predictions. Recent advances in modeling of carbon allows for the calculation of the phase diagram of carbon and the structure of the liquid with unprecedented accuracy. This provided significant progress in the understanding of the behavior of carbon under extreme conditions [26–30]. Knowledge of the location of the melting line and the liquid structure near melting is an important requisite in understanding the (non)-existence of a liquid–liquid phase transition and the process of homogeneous nucleation of the liquid into graphite or diamond. The latter issue is key to answering the question of the existence of diamond in planet interiors.

In the present contribution we provide a review of some of the recent computational studies of the phase diagram and the liquid structure of carbon. First, we summarize some important characteristics of the carbon phase diagram. Then we discuss the modeling of the inter-atomic interaction with a focus on a particular class of bond-order potentials, the so-called LCBOP models. Subsequently we discuss in detail the computational methods to determine the thermodynamic stability of the diamond, graphite, and liquid phase together with a presentation of the calculated phase diagram for a well tested version of the LCBOP model. These results are discussed in a context of experimental and other computational studies. Finally, we address the structure of liquid carbon.

1.2 Carbon Phase Diagram: Some Important Characteristics

In the pressure and temperature range up to 100 GPa and 10,000 K, the well established thermodynamic stable phases of carbon are the crystalline graphite (G) and diamond (D) phase at lower temperatures, and a liquid (L) phase at higher temperatures (Fig. 1.4). The graphite-diamond coexistence line has been relatively well characterized up to 2,400 K [7, 15]. For the graphite melting line a large amount of experimental data are available [1, 8, 9, 13, 14, 16]. The experiments have in common that the melting temperature shows little variation with pressure, and that most of the measured graphite melting $P - T$ lines [8, 9, 16] show a maximum around $P = 6$ GPa. However, the nature of the maximum is not well established. The experimental estimates for the melting temperatures show a large spread. It appears that the estimated melting temperature depends significantly on the heating rate of the sample [13, 14], yielding values from 3,700 to 5,000 K below 0.01 GPa. In a recent comprehensive review of graphite melting [31] the melting temperature is proposed to be in the range of 4,600–5,000 K. The precise nature of the maximum in the melting curve is important, because a discontinuous change of slope of the melting curve

at this point would imply the existence of a liquid–liquid phase transition (LLPT) line, branching off from the graphite melting curve. This will be discussed in more detail in Section 1.5.

Early shock wave experiments [11] provided evidence for the existence of diamond at $P = 140$ GPa at a temperature beyond the temperature of the Graphite–Diamond–Liquid triple point (T $\sim$ 4,000 K), implying that the carbon diamond melting line has a positive slope in the $P - T$ diagram. Recent experimental data have provided evidence [32] that diamond is stable up to at least 800 GPa.

1.3 Modeling Carbon

Realistic modeling of the carbon phase diagram involving the liquid, graphite, and diamond phase requires an accurate description of the inter-atomic interactions, combined with a precise evaluation of the relative stability of the involved phases. This requires the evaluation of the free energy of state points in all phases involved. Presently, density-functional theory (DFT) based ab initio MD simulations would provide the best possible approach. However, the computational cost associated with DFT calculations renders such an approach unfeasible, in particular when combined with free-energy calculations.

A viable alternative is to model the inter-atomic interactions by a functional description, whose parameters are (partly) fitted to a selected database. Such a functional description (also referred to as empirical, semi-empirical or classical potentials) serves several purposes, ranging from the modeling of minimum energy structures for surface reconstructions, grain boundaries or related defects, to the description of the liquid structure and thermodynamic stability.

According to Brenner [33], an analytic potential needs to be:

- *Flexible* The function should be flexible enough to accommodate the inclusion of a relatively wide range of structures in a fitting database.
- *Accurate* The potential function must be able to accurately reproduce quantities such energies, bond lengths, elastic constant, and related properties entering a fitting database.
- *Transferable* The functional form of the potential should be able to reproduce related properties that are *not* included in the fitting database. In practice the potential should be able to give a good description of the energy landscape for any possible realistic configuration characterized by the set of atomic positions $\{\mathbf{r}_i\}$.
- *Computationally Efficient* The function should be of such a form that it is tractable for a desired calculation, given the available computing resources.

Focusing on carbon, there is a noble lineage of increasingly successful parameterizations of the empirical potentials, from the Tersoff [34] potential, via the Brenner potentials [35] and their modifications [36–39] up to Los-Fasolino LCBOP [27,29]. The crucial characteristic of these potentials is that they account for the "bond order" : the potentials formalize and parameterize the idea that for covalently bonded

systems an increasing number of bonds per atom modifies (typically decreases) the bond energy *per bond*. With increasing complexity, many-body contributions due to angular correlations [34], conjugation effects [35] and torsional interactions [36] were included. These short ranged potentials proved to describe increasingly well hydrocarbon molecules (when hydrogen is included) and the diamond phase. However, more disordered structures were less well described. After an earlier attempt to introduce longer range (pair) correlations [38], the seamless inclusion of non-bonded interactions led to the semi-empirical long range bond order potential (LCBOPI) by Los and Fasolino [27] that is partly based on ab initio data. The inclusion of conjugation dependent torsional interactions (LCBOPI$^+$) (Ref. [29] in Appendix A, and Ref. [40] in chapter 6.7) added the necessary flexibility to describe in a proper way the transformation between diamond and graphite and the structure of the liquid phase. LCBOPI$^+$ also accounts properly for the inter-planar interactions in graphite. In a subsequent development, the introduction of middle range interactions (i.e. allowing for smooth bond breaking and forming), together with a revision of the definition of the torsional angle, yielded LCBOPII [29], which performs as well as density functional in the liquid phase (wherever it was tested) and opens the way for an accurate description of surfaces and their reconstructions.

The LCBOP family is the first empirical potential that is capable of providing an accurate description of the graphite, diamond, and liquid phase. This makes the LCBOP's uniquely suited to predict the carbon phase diagram and the properties of liquid carbon.

1.4 The Graphite–Diamond–Liquid Phase Diagram of LCBOPI$^+$

1.4.1 Computational Methods

The properties of the liquid, graphite, and diamond phases were determined by Monte Carlo (MC) simulations. Coexistence lines were determined by locating points in the $P - T$ diagram with equal chemical potential for the two phases involved. To this purpose, we first determined the chemical potential for the liquid, graphite, and diamond at an initial state point ($P = 10$ GPa, $T = 4{,}000$ K). Subsequently, the liquid/graphite, liquid/diamond, and graphite/diamond coexistence pressures at $T = 4{,}000$ K were located. In turn, these coexistence points served as the starting point for the determination of the graphite melting, diamond melting, and graphite/diamond coexistence lines, obtained integrating the Clausius–Clapeyron equation (this procedure is also known as Gibbs–Duhem integration):

$$\frac{\mathrm{d}T}{\mathrm{d}P} = \frac{T\Delta v}{\Delta h} \tag{1.1}$$

where Δv is the difference in specific volume, and Δh the difference in molar enthalpy between the two phases (calculated as $h = u + Pv$, being u the potential energy per particle).

The first point is in turn accomplished in two sub-steps. Firstly a Helmholtz free energy (F) at a given volume (V) and temperature (T) can be calculated via thermodynamic integration. In a canonical system, coexistence between phases can be found via the Helmholtz double tangent construction, after F is evaluated at other V and T, by integrating its gradient, a quantity that can be measured in a MC simulation (see e.g. Ref. [21]). As an alternative [41], the one we chose, one can transform F into the chemical potential μ (coinciding with the specific Gibbs free energy in a one-component system), the latter as a function of P and T, knowing accurately enough the equation of state of each phase. Coexistence at a given T is found at that P where μ for the different phases cross.

For all phases, the free energies at the initial state point F^{Ξ} was determined by transforming the systems into a reference system F^{ref} of known free energy, using $U_\lambda = (1-\lambda)U^{\Xi} + \lambda U^{\mathrm{ref}}$. Here, U^{Ξ} and U^{ref} denote the potential energy function of the LCBOPI$^+$ and of the reference system, respectively. The transformation is controlled by varying the parameter λ continuously from 0 to 1. The free-energy change upon the transformation was determined by thermodynamic integration:

$$\begin{aligned} F^{\Xi} &= F^{\mathrm{ref}} + \Delta F^{\mathrm{ref}\to\Xi} \\ &= F^{\mathrm{ref}} + \int_{\lambda=0}^{\lambda=1} d\lambda \left\langle \frac{\partial U_\lambda}{\partial \lambda} \right\rangle_\lambda \\ &= F^{\mathrm{ref}} + \int_0^1 \mathrm{d}\lambda \left\langle U^{\mathrm{ref}} - U^{\Xi} \right\rangle_\lambda \end{aligned} \tag{1.2}$$

The symbol $\langle ... \rangle_\lambda$ denotes the ensemble average with the potential U_λ.

For the liquid phase the reference system was taken to be a Lennard–Jones 12-6 (LJ) system, described by the well known interaction energy:

$$U^{LJ} = 4\varepsilon \left(\left(\frac{\sigma}{r}\right)^{12} - \left(\frac{\sigma}{r}\right)^{6} \right)$$

The reference free energy (F^{ref}) of the liquid is:

$$F^{\mathrm{ref}} = F^{\mathrm{LJ}} = F^{\mathrm{id}} + F^{\mathrm{ex}}_{\mathrm{LJ}} \tag{1.3}$$

The ideal-gas contribution is:

$$\frac{\beta F^{\mathrm{id}}}{N} = 3\ln\Lambda + \ln\rho - 1$$

where N is the number of particles in the box, $\Lambda = h/\sqrt{2\pi m k_B T}$ is the de Broglie wavelength, m is the mass of one atom, and ρ is the number density. The LJ liquid excess free energy ($F^{\mathrm{ex}}_{\mathrm{LJ}}$) has been accurately parameterized [42] by means of (NVT) MC and MD simulations.

The LJ σ parameter was determined by matching the first peak of the radial distribution functions ($g(r)$) of the LCBOPI$^+$ and LJ liquid at the same position, ensuring optimal similarity between the structure of the two liquids. The LJ ε parameter was chosen such that, at the selected $T = 4{,}000\,\mathrm{K}$, the LJ liquid was above the critical temperature: this is done in order to avoid possible unwanted transitions, since the thermodynamic integration method works under the hypothesis that no boundary between phases is ever crossed on varying λ. On the other hand, the liquid should not be too far from the critical temperature: in fact, the $g(r)$ given by the LCBOPI$^+$ (see Section 1.5) has pronounced secondary peaks beyond the first coordination shell. Thus, a rather structured LJ liquid had to be preferred for the coupling. The requirements are matched by putting the LJ liquid in proximity of the critical temperature.

For the solid phases the Einstein crystal, whose free energy is analytically known, was taken as reference system [43]. For the Einstein solid, U^E is:

$$U^E = \frac{\alpha}{2} \sum_{i=1}^{N} (\mathbf{r}_i - \mathbf{r}_{i,0})^2$$

where the $\mathbf{r}_{i,0}$ are the equilibrium (i.e. at $T = 0\,\mathrm{K}$) lattice positions of the particles. In the Einstein solid, the fixed equilibrium lattice positions are referred to an absolute frame, so that if a particle is moved, then the crystal as a whole cannot. When $\lambda \sim 0$ (i.e. the system is on the LCBOPI$^+$ side) the center of mass of the system (CoM) is free to drift: if L is the box size, the CoM mean square displacement $\langle r^2 \rangle_{CoM}$ becomes of the order of L^2. Should this happen, the integral of Eq. 1.2 becomes sharply peaked for small values of λ. In fact, the particles are allowed to drift far away from their absolute equilibrium lattice positions, since the coupling with the Einstein solid is mild, but in Eq. 1.2 appears the energy $U^{\Phi} = U^E$, that can become uncontrollably large. In order to circumvent this problem for small λ, a physically well founded remedy is to perform a simulation under the constraint that the CoM of the solid is fixed [43–45], so that $\langle r^2 \rangle_{CoM}$ is of the order of $\langle r^2 \rangle_0$, the mean square displacement of a particle from its lattice site in a real (i.e. interacting) crystal. This constraint calls for a slight modification of Eq. 1.2. We label with $E(CM)$ the Einstein solid with fixed center of mass, $\Phi(CM)$ the LCBOPI$^+$ system with fixed center of mass, so that [43–45]:

$$\begin{aligned} F^{\Phi} &= F^{\mathrm{E(CM)}} + \Delta F^{\mathrm{E(CM)} \to \Phi(CM)} + \Delta F^{\Phi(\mathrm{CM}) \to \Phi} \\ &= F^{\mathrm{E(CM)}} + \int_0^1 \mathrm{d}\lambda \left\langle U^{\mathrm{ref}} - U^{\Phi} \right\rangle_{\lambda} + \Delta F^{\Phi(\mathrm{CM}) \to \Phi} \end{aligned} \tag{1.4}$$

Specifically:

$$\frac{\beta F^{\mathrm{E(CM)}}}{N} = 3\ln\Lambda - \frac{3}{2}\ln\left(\frac{2\pi}{\beta\alpha}\right) - \frac{3}{2N}\left(\ln\left(\frac{\alpha\beta}{2\pi}\right) + \ln N\right) \tag{1.5}$$

The last term on the right hand side represents the (finite size) correction for the fixing of the CoM. Note its dependency on $1/N$, which consistently makes the correction vanish in the thermodynamic limit.

$$\frac{\beta\Delta F^{\Phi(\mathrm{CM})\to\Phi}}{N} = -\frac{1}{N}\ln\frac{V}{N_{ws}} \tag{1.6}$$

where N_{ws} is the number of Wigner–Seitz cells in the simulation box. If n_{ws} is the number of atoms per Wigner–Seitz cell, $N_{ws} = N/n_{ws}$. Note that also this term, a purely finite size effect, vanishes in the thermodynamic limit.

In reporting the results (in Section 1.4.2) we will group differently the terms of the previous three equations: it is indeed natural to group the terms proportional to $\frac{1}{N}$, so that:

$$\frac{\beta F^{\mathrm{E}}}{N} = 3\ln\Lambda - \frac{3}{2}\ln\left(\frac{2\pi}{\beta\alpha}\right) \tag{1.7}$$

$$\frac{\beta\Delta F^{\frac{1}{N}}}{N} = -\frac{1}{N}\left(\frac{3}{2}\ln\left(N\,\frac{\alpha\beta}{2\pi}\right) + \ln\frac{V}{N_{ws}}\right) \tag{1.8}$$

The coupling of (hot) graphite to an Einstein crystal, whose average atomic positions are constrained to a fixed reference system, displayed a peculiar feature. Due to the softness of the interplanar interactions (0.07 $\mathrm{k_B T}$ at 4,000 K), graphite neighboring sheets are allowed to slide. Also this is a finite size effect: to correct for this we found necessary to attach any sheet to its CoM, independently from the others.[1]

The Einstein crystal spring constant, α, was determined by requiring that the mean-squared displacement from the equilibrium lattice positions is equal for the Einstein crystal and the carbon crystal:

$$\frac{3}{\beta\alpha} = \left\langle \frac{1}{N}\sum_{i=1}^{N}(\mathbf{r}_i - \mathbf{r}_{i,0})^2 \right\rangle$$

Therefore α was fixed by calculating the right hand side in a simulation with the LCBOPI$^+$.

[1] Equation 1.5 then becomes:

$$\frac{\beta F^{\mathrm{E(CM)}}}{N} = 3\ln\Lambda - \frac{3}{2}\ln\left(\frac{2\pi}{\beta\alpha}\right) - \frac{3N_s}{2N}\left(\ln\left(\frac{\alpha\beta}{2\pi}\right) + \ln N N_s\right)$$

where N_s is the number of sheets. Equation 1.6 becomes:

$$\frac{\beta\Delta F^{\Phi(\mathrm{CM})\to\Phi}}{N} = -\frac{N_s}{N}\ln\frac{V}{N_{ws}}$$

where, in $N_{ws} = N/n_{ws}$, one has to define the Wigner–Seitz cell within a graphite sheet; this leads to $n_{ws} = 2$. Equation 1.8 becomes:

$$\frac{\beta\Delta F^{\frac{1}{N}}}{N} = -\frac{N_s}{N}\left[\frac{3}{2}\ln\left(N N_s\,\frac{\alpha\beta}{2\pi}\right) + \ln\frac{V}{N_{ws}}\right].$$

Table 1.1 Parameters for the polynomial fitting of the 4,000 K isotherms of the three phases, according to: $P(\rho) = a + b\rho + c\rho^2$

	a [GPa]	b [GPa nm^3]	c [GPa nm^6]
Liquid	89.972	−1.9654	0.011 092
Diamond	74.809	−3.6307	0.019 102
Graphite	108.29	−2.2707	0.011 925

In order to estimate the chemical potential μ along the 4,000 K isotherm we integrated from the initial state point a fit, $P(\rho) = a + b\rho + c\rho^2$, through simulated (P, T) state points along the 4,000 K isotherm. Here, ρ is the number density, and a, b, and c are fit parameters (see Table 1.1). This yields for the chemical potential [41]:

$$\beta\mu(\rho) = \frac{\beta F^{\Rightarrow}}{N} + \beta\left[\frac{a}{\rho^{\Rightarrow}} + b\,\ln\frac{\rho}{\rho^{\Rightarrow}} + b + c\left(2\rho - \rho^{\Rightarrow}\right)\right] \tag{1.9}$$

Here, $\rho^{\Rightarrow}$ denotes the number density at the initial state point, N the number of particles, and $\beta = 1/k_{\mathrm{B}}T$, with k_{B} the Boltzmann constant. Details on this equation are given in Appendix A.

1.4.2 The LCBOPI$^+$ Phase Diagram

For calculating the three $F^{\Rightarrow}$ we performed independent Monte Carlo (MC) simulations for three phases. Three samples of 216 particle of the three systems were prepared, the solids in their lattice positions, and the liquid in a simple cubic arrangement. The three phases were equilibrated with NPT MC simulations at the chosen $T = 4{,}000$ K and at $P = 10$ GPa.[2] The integer N = 216 permits the atoms to be arranged both in a defect-free diamond and cubic lattice, aligned with the sides of a cubic cell, while bonding perfectly across its faces to periodic-image atoms. The same requirements are fulfilled for 216 atoms in a defect-free graphite lattice, arranged in three sheets, but in a rectangular periodically replicated cell, with resulting edge-size ratios 1:1.5:1.7. The first, in-plane, ratio (1:1.5) is defined by the lattice geometry (hexagons), while the interplanar ratio (1:1.7) is pressure dependent. In fact, the rescaling of the box was allowed to be independent on the three axes for the equilibration of the solid phases, while kept intrinsically isotropic for the melting of the cubic crystal and the subsequent equilibration of the liquid phase. The equilibrium densities $\rho^{\Rightarrow}$, expressed in 10^3 kg/m^3, were 3.425 for diamond, 2.597 for graphite, and 2.421 for the liquid. Three configurations at the equilibrium volume were then chosen as starting points for the three thermodynamic integrations. The value of α

[2] For the correct application of the method it is not needed to have the three states at the same P. It is only required that the phases share a broad stable region in pressure at the chosen T.

was set to 453,000 and 39,700 kJ/(mol nm^2) for diamond and graphite, respectively. The parameters σ and ε for the LJ fluid were 0.127 nm and 31.84 kJ/mol.

The reference free energies $\beta F^{\mathrm{E}}/N$ were $-5.755\ k_BT$, and $-1.912\ k_BT$ for graphite and diamond, respectively, while the reference free energy for the liquid was found $(\beta/N)\left(F^{\mathrm{id}} + F^{\mathrm{ex}}_{\mathrm{LJ}}\right) = -10.863\ k_BT$. The integration in Eq. 1.2 yields for $\beta F^{\Phi}/N$ the values $-25.090 \pm 0.006\ k_BT$ (graphite), and $-24.583 \pm 0.002\ k_BT$ (diamond), $-25.137 \pm 0.002\ k_BT$ (liquid).

The values of λ for the sampling were defined by a 10-point Gauss–Legendre integration scheme. The scheme avoids the sampling of the systems at the two boundary values of λ. A 10 point scheme assures exact result whenever the integrand function of Eq. 1.2 $\left(\langle U^{\mathrm{ref}} - U^{\mathrm{LCBOPI}^+}\rangle_\lambda\right)$ can be reasonably described with a polynomial up to order $2 * 10 + 1 = 21$. When $\lambda = 0, 1$ the system performs its random walk on the basis of only one of the two potentials, thus in principle is allowed to assume configurations completely avoided by the other potential, in such a way that the integrand of Eq. 1.2 could diverge. Should this be the case, the integration scheme would yield a poor estimate of the integral. We thus ascertained that the integrand never indeed diverged at $\lambda = 0, 1$. For the three phases, we run at each λ point an NVT MC simulation of 500,000 cycles.

In Fig. 1.1 $\langle U^{\mathrm{ref}} - U^{\mathrm{LCBOPI}^+}\rangle_\lambda$ versus λ is shown. The absence of spurious phase boundary crossings throughout the integration over λ was checked by looking at the

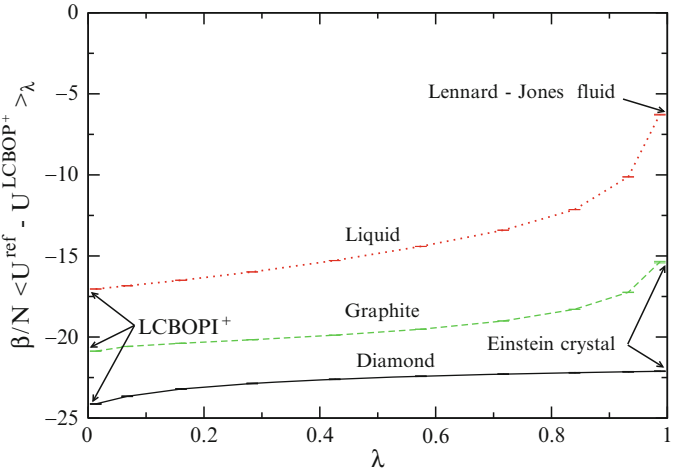

Fig. 1.1 Plots of the quantity $\beta/N\ \langle U^{\mathrm{ref}} - U^{\mathrm{LCBOPI}^+}\rangle_\lambda$ (see Eqs. 1.2 and 1.4) as a function of the coupling parameter λ for the liquid, graphite, and diamond phase. On the *left side* of the horizontal axis ($\lambda = 0$) is the pure LCBOPI$^+$. On the *right side* ($\lambda = 1$) is the reference system, i.e. the Lennard–Jones liquid for the liquid phase and two Einstein crystals (with different coupling constant) for graphite and diamond phase. The temperature is 4,000 K and the pressure is 10 GPa for the three phases, at $\lambda = 0$ (along the integration path the volume, rather than the pressure, is conserved). The simulated λ-points are marked by their *error bars*, that are almost reduced to a single dash at this scale

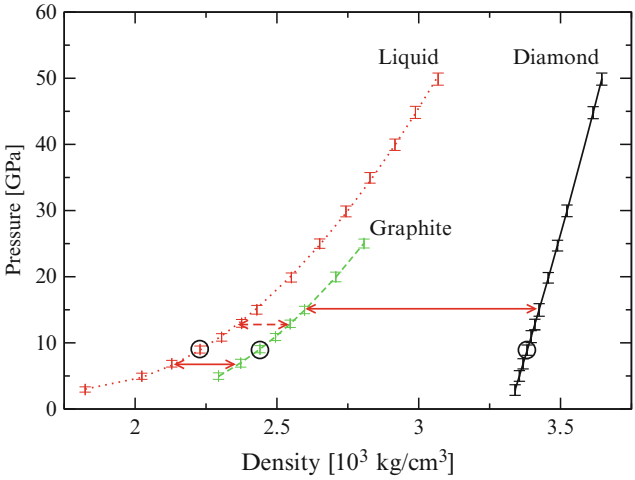

Fig. 1.2 Equations of state at 4,000 K for the liquid, graphite, and diamond phase. The *lines* are the quadratic polynomial fits to the data. The *circles* indicate the points, at 10 GPa, where the thermodynamic integration (Eq. 1.2) was performed. The *solid arrows* connect coexisting (stable) points, i.e. liquid/graphite and graphite/diamond. The *dashed arrow* links the liquid/diamond coexisting point, that is metastable relative to the graphite phase

distribution of $(U^{\text{ref}} - U^{\text{LCBOPI}^+})$.[3] Since the points were run in parallel in order to accumulate more statistics, only shorter independent simulations were performed by increasing and then decreasing λ, each new λ point starting from the final configuration of the previous. The absence of hysteresis in this process completely rules out phase boundary crossings. The isotherms for the three phases, calculated via NPT MC simulations together with their fit, are shown in Fig. 1.2.

The three μ curves (at $T = 4{,}000$ K), as given in Eq. 1.9, but expressed as functions of P, are shown in Fig. 1.3. The three curves, μ_{L}, μ_{G}, μ_{D}, as given in Eq. 1.9, intersect in pairs in three points (these points are shown as a solid triangle, square and diamond in Fig. 1.4). The intersections locate the graphite/liquid coexistence at 6.72 ± 0.60 GPa ($\mu_{\text{GL}} = -24.21 \pm 0.10\ k_{\text{B}}T$), and the graphite/diamond coexistence at 15.05 ± 0.30 GPa ($\mu_{\text{GD}} = -23.01 \pm 0.03\ k_{\text{B}}T$). The third intersection locates a diamond/liquid coexistence at $= 12.75 \pm 0.20$ GPa ($\mu_{\text{DL}} = -23.24 \pm 0.03\ k_{\text{B}}T$). Even though both diamond and the liquid are there metastable, this point can be taken as the starting one for the Clausius–Clapeyron integration of the diamond melting line. Starting from the three coexistence points at 4,000 K, the coexistence lines were traced–by integrating the Clausius–Clapeyron equation using the trapezoidal-rule predictor-corrector scheme [46]. The new value of the coexisting P at a given T was taken when two iterations differed less than 0.01 GPa, this being the size of the single uncertainty in the calculation of $\mathrm{d}P/\mathrm{d}T$. This normally took two to three iterations to be obtained.

[3] The distribution usually exhibits a bimodal shape in case of phase boundary crossing.

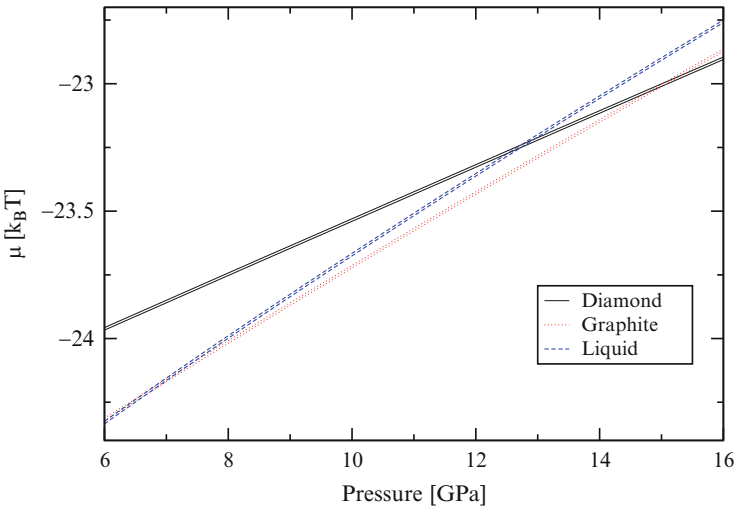

Fig. 1.3 Plot of the chemical potential μ for the three phases at $T = 4{,}000$ K; we plot *double lines*, which marks the boundaries of the numerical uncertainty of the calculated μ. These curves represent Eq. 1.9, but are expressed as a function of pressure using $P(\rho) = a + b\rho + c\rho^2$. The main source of error was the thermodynamic integration; the uncertainty in the equations of state was at least an order of magnitude less

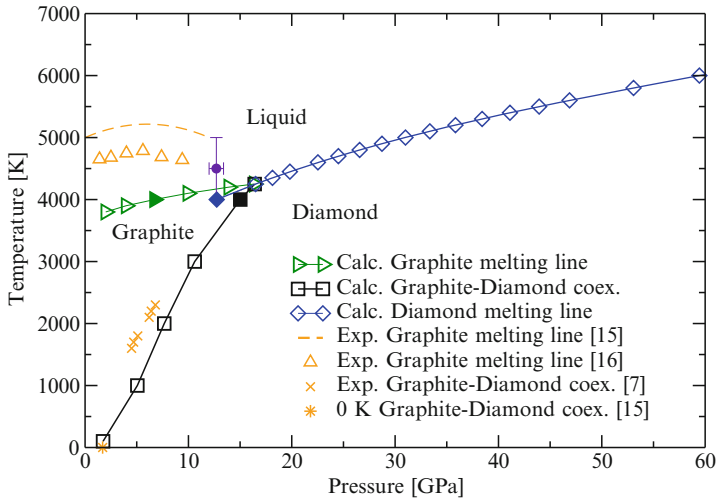

Fig. 1.4 Phase diagram of carbon up to 60 GPa. The *solid right triangle*, *square*, and *diamond* are the three coexistence points found by equating the chemical potentials at 4,000 K (see text). The *open right triangles*, *squares*, and *diamonds* are the calculated coexistence points, propagated via Gibbs–Duhem integration. The *solid circle* with *error bars* indicates the experimental estimate for the liquid/graphite/diamond triple point [15, 18, 20]. The *dashed line* is the experimental graphite *melting line* from Ref. [15]. The *up triangles* are graphite melting state points from Ref. [16]. The *crosses* represent experimental graphite/diamond coexistence from Ref. [7]. The *asterisk* represent the theoretical graphite/diamond coexistence at zero kelvin, as reported in Ref. [15]

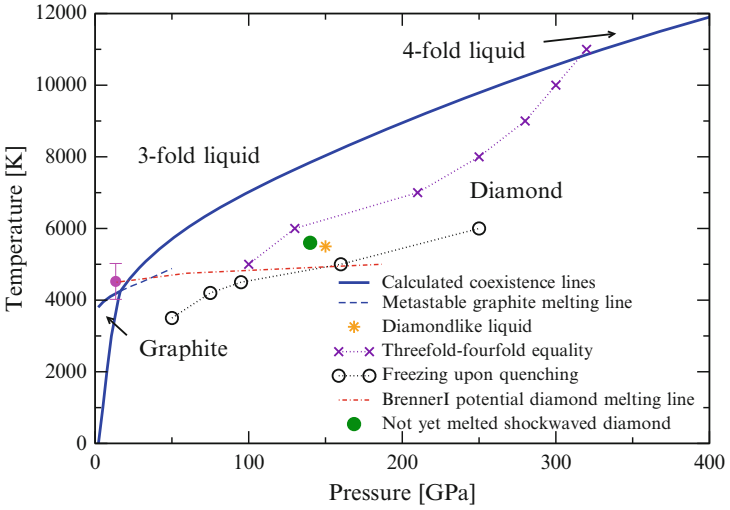

Fig. 1.5 Phase diagram of carbon at all calculated pressures. The thick *solid lines* are the calculated phase boundaries. The *dashed line* is the metastable prolongation of the graphite *melting line*, from Gibbs–Duhem integration; the line stops just before the simulated graphite became instable, displaying large density fluctuations. The *dashed-dotted line* departing from the experimental guess for the triple point (*solid circle* with *error bar* [15,18,20]) is the diamond *melting line* calculated in Ref. [21] with the BrennerI potential. The *solid circle* is the final point of the shock wave experiment of Ref. [11] at which diamond is not yet melted. Crosses mark the liquid with equal amount of three- and fourfold atoms; *circles* represent state points in which the sample freezes; in the region in between the two series is the "diamond-like liquid": the star is the point reported in Ref. [47]

Table 1.2 Pressure (P), temperature (T), solid and liquid densities (ρ) along the melting lines

P [GPa]	T [K]	ρ_G [10^3 kg/m^3]	ρ_L [10^3 kg/m^3]
Graphite melting line:			
2.00	3,800	2.134	1.759
6.70	4,000	2.354	2.098
16.4	4,250	2.623	2.414
Diamond melting line:			
16.4	4,250	3.427	2.414
25.5	4,750	3.470	2.607
43.9	5,500	3.558	2.870
59.4	6,000	3.629	3.043
99.4	7,000	3.783	3.264
148.1	8,000	3.960	3.485
263.2	10,000	4.286	3.868
408.1	12,000	4.593	4.236

The calculated phase diagram in the $P - T$ plane is shown in Fig. 1.4 for the low pressure region, and in Fig. 1.5 for the full range of pressures and temperatures considered. Table 1.2 lists the densities of selected points on the coexistence lines. The three coexistence lines meet in a triple point at 16.4 $\pm$ 0.7 GPa and 4,250 $\pm$ 10 K.

Table 1.3 Pressure (P), temperature (T), and melting enthalpy (Δh_m, calculated as the enthalpy of the liquid subtracted of the enthalpy of the underlying solid phase) along the melting lines

P [GPa]	T [K]	Δh_m [kJ/mol]
Graphite melting line:		
2.00	3,800	68.8
5.24	3,950	65.6
9.94	4,100	67.8
16.4	4,250	64.7
Diamond melting line:		
16.4	4,250	95.9
25.5	4,750	111.5
43.9	5,500	130.8
59.4	6,000	143.9
99.4	7,000	160.5
148.1	8,000	174.7
263.2	10,000	195.3
330.5	11,000	208.1
408.1	12,000	221.7

The graphite/diamond coexistence line agrees very well with the experimental data. In the region near the liquid/graphite/diamond triple point, that has not been directly probed in experiments, the graphite/diamond coexistence line bends to the right, departing from the usually assumed straight line. Analysis of our data shows this is mainly due to the fast reduction with increasing pressure of the interplanar distance in graphite at those premelting temperature. This causes an enhanced increase of the density in graphite, yielding a decrease of $\mathrm{d}T/\mathrm{d}P$.

Table 1.3 shows the melting enthalpy Δh_m for graphite and diamond. These are calculated as the difference in enthalpy between the solid and the melt at coexistence. Our calculated melting enthalpies of graphite are sensibly lower than the values around 110 kJ/mol reported in shock heating melting experiments in the past years [15, 16], nonetheless our values retain the feature of being rather constant along the graphite melting line. No experimental data are known about the melting enthalpies of diamond: we note that they increase monotonically with temperature (and pressure).

The calculated graphite melting line is monotonically increasing in a small temperature range around 4,000 K. In contrast to data inferred from experiments it shows no maximum and is at a somewhat lower temperature. In agreement with the experiments the coexistence temperature is only slowly varying with pressure. Inspection reveals that this behavior is due to (1) the limited variability of the melting enthalpy, and (2) a similar bulk modulus for liquid and graphite such that Δv is almost constant.

We have extended the calculation of the graphite melting line to the region in which both graphite and the liquid are metastable towards diamond, with the aim to look for a possible maximum in the line. The results are shown as a dashed line in Fig. 1.5. We stopped the Gibbs–Duhem integration at $\sim$50 GPa, where the 216-particles graphite sample started showing huge volume fluctuations during the NPT sampling. The integration algorithm became instable, forbidding any further analysis. Looking at this metastable melting line, it is clear that its slope does not

continue to decrease with increasing pressure as in the stable region; thus, the hypothesis of an hidden maximum appears to be rejected.

The slope of the diamond melting line is consistent with the only experimental point available [11] (see Fig. 1.5). When compared to the diamond melting line of the Brenner model [21], the LCBOPI$^+$ diamond melting line has a steeper slope yielding significantly higher temperatures for the diamond melting line.

1.4.3 Diamond Melting According to LCBOPII

We have not carried out an extensive numerical evaluation of the phase diagram as predicted by the LCBOPII. Yet, using direct free-energy difference calculations starting from the diamond melting line of the LCBOPI$^+$, we determined one point and the slope at that point of the diamond melting line for the LCBOPII. We sampled with the LCBOPI$^+$ a liquid and a diamond sample at the same phase point on the calculated diamond melting line and at intervals a virtual swapping between the two potentials, LCBOPI$^+$ and LCBOPII, was performed. This means that the energy of independent configurations during this run was evaluated also with the LCBOPII. We chose $T_m = 6{,}000$ K, which gave $P_m = 59.44$ GPa for the coexistence for the LCBOPI$^+$. We found for LCBOPII $T_m = 5{,}505$ K at the same pressure. The slope of the melting line was evaluated by means of the Clausius–Clapeyron equation. We found a slope of 28.04 K/GPa. We compare it to the very close value of 28.97 K/GPa as given by the LCBOPI$^+$ at the same pressure. Thus, by means of this single point evaluation, we found that LCBOPII has a melting line at lower temperature than the LCBOPI$^+$, but the slope should be similar between the two potentials.

1.4.4 Recent Developments

Recently, the melting curve of diamond in a range up to 2,000 GPa has been studied by ab initio MD simulations using density functional theory. Wang et al. [48] determined the relative stability of the diamond and liquid phase by evaluating the free energy of both phases. Correa et al. [26] determined the melting temperature using a "two phase" simulation method, where the system initially consists of a liquid and a diamond structure that are in contact. Subsequently the melting temperature is estimated by locating the temperature at which the system spontaneously evolves towards a liquid or a crystalline structure. In both ab initio MD studies it was found that the diamond melting curve shows a maximum; around 450 GPa [26] or 630 GPa [48].[4] Subsequent laser-shock experiments [49] provided data consistent

[4] The difference between these two values gives a hint on the uncertainties related to the two different methods used for calculating coexistence, given that the DF-MD set-up is quite similar in the two works.

with this observation, indicating a negative melting slope most probably in the region of 300–500 GPa. When comparing the LCBOPI$^+$ diamond melting curve, that monotonically increases with pressure, to the ab initio MD results of Refs. [26, 48] we see a significant deviation from 200 GPa onwards. This might be attributed to an incorrect description of the liquid structure at high compression. Indeed, LCBOPI$^+$ has not been validated against high density structures with coordination beyond four. These are typical configuration that might become more dominant in the pressure region beyond 200 GPa.

1.5 The Nature of Liquid Carbon: Absence of a *First-Order* Liquid–Liquid Phase Transition

In this section we re-examine the issue of the liquid–liquid phase transition (LLPT) for carbon. A short review of the relevant findings is given in Section 1.5.1. In Section 1.5.2 we describe the liquid at 6,000 K as predicted by several bond order potentials (see Fig. 1.9 for the complete list) and compare the results with density functional (DF) based molecular dynamics (MD) calculation. The temperature was chosen to agree with the DF-MD based analysis of the liquid Wu et al. [22] There the isotherm at 6,000 K was originally chosen for two reasons. Firstly it is expected to be far from coexistence in the density interval studied; this assumption is based on the phase diagram calculated by Glosli and Ree [21] using one of the Brenner bond order potential [35] (the authors do not specify which parameterization they use). Secondly, the 6,000 K isotherm is predicted by Glosli and Ree [20], with the BrennerI [35] bond order potential, to cross the liquid–liquid coexistence line. In Section 1.5.3 the analysis will be extended at all the relevant regions of the phase diagram, with the aim of ruling out the presence of a LLPT, at least within the scope of the LCBOP family. Intriguingly, signatures of a LLPT transition are nonetheless hinted at by LCBOPII for the strongly undercooled liquid, where the liquid would be anyhow dynamically arrested into a glass (see Section 1.5.2.3). A characteristic that carbon would share with water.

1.5.1 A Short History of Carbon LLPT

An Analysis of Experimental Data The possibility of a liquid–liquid phase transition (LLPT) in liquid carbon has been firstly investigated by Korsunskaya et al. [17], analyzing data on the graphite melting line proposed by Bundy [8] (those data showed a maximum melting temperature at 6.5 GPa). By fitting the data from Bundy into the original two levels model of Kittel [50] and postulating the existence of two liquids, Korsunskaya et al. found the critical temperature T_c of the LLPT. The

model is fitted with three points on the graphite melting line, with the respective derivatives, and with the heat of melting at a selected pressure. The authors assume that:

1. Liquid and solid have different compressibilities.
2. The nature of liquid carbon is described univocally by the relative fraction of the two liquids.
3. Each of the two liquids presents a volume change on melting, heat of melting and entropy of melting that are independent of T, P, and the fraction s: the volume change upon melting for the liquid is a linear combination of the volume changes of the pure species (i.e. for $s = 0, 1$), while heat and entropy of melting combine according to the regular solution rules.
4. The overall entropy jump on melting is independent of T (that is equivalent to assuming the same heat capacity in the liquid and the solid).

The fitting procedure gives an estimate for the critical pressure of ∼6.5 GPa and for the critical temperature of the searched transition at 3,770 K, i.e. below the melting temperature. The fitted value for the entropy of melting is the same for the two liquids, thus implying a vertical slope ($\mathrm{d}T/\mathrm{d}P$) of the coexistence line (in the metastable liquid region just below the critical temperature).

When the slope of two out of the three coexisting line meeting at a triple point is known, the slope of the third is also determined. On the basis of their results, the authors were thus able to calculate also the diamond melting line: they predicted it to have a negative slope. Note that the slope of the *graphite* melting line, and the slope of the diamond/graphite coexistence, as extracted from Bundy's data [7, 8], together with the densities of the phases obtained by fitting to the two levels model *implied* (via Clausius–Clapeyron equation) a negative slope of the diamond melting line. Different values of the slopes of the graphite boundary lines, and of the densities of the phases can yield rather different slope of the diamond melting line, as we have shown in Section 1.4.

Consistently with the slope of the fitted graphite melting line, the low density liquid (LDL, $s = 0$) is less heavy, and the high density liquid (HDL, $s = 1$) is heavier than the coexisting graphite. The nature of the two liquids is predicted as follows: at low pressure graphite melts into a liquid of neutral particles, which interact predominantly through dispersion (London) forces. Upon increasing pressure[5] the liquid metallizes into a close packed liquid. No assumption is made on the local structure.

A Semi-empirical Equation of State The modern discussion on the LLPT for carbon, starts with the elaboration of a semi-empirical equation of state for carbon, valid also at high P and T, by van Thiel and Ree [18, 51]. The equation of state is constructed on the basis of experimental data and electronic structure calculations. It is postulated the existence, in the graphite melt, of a mixture of a threefold (sp_2) and

[5] The transition in the stable liquid region is supercritical, thus continuous, but taking place in a short range of pressures around 6.5 GPa.

a fourfold (sp_4) liquid. The model of *pseudo-binary mixture* is assumed to describe the mixing of the two liquids [52]; the mixing energy J of the two liquids is written as: $\beta J = \left[A_0/\left(1 + (P/P_0)^{3/2}\right)\right] s(1-s)$ where $\beta = 1/(k_B T)$, A_0 and P_0 are fitting parameter, and s is the fraction of the sp_3 liquid. The value of these fitting parameters is essential to determine the possibility of the occurrence of a first order transition. Van Thiel and Ree show that fitting A_0 in order to obtain the graphite melting points of Bundy [8], the slope of the graphite melting line predicted by their model inverts its sign discontinuously in correspondence of the maximum, so that a first order LLPT arises. On the other hand, if they fit to the data from Ref. [9], the value of A_0 decreases so that the T_c of the LLPT drops below the melting line and the transition between the two liquids becomes continuous in the stable liquid region. As pointed out by Ponyatovsky [53] the expression for βJ proposed by van Thiel and Ree involves two ambiguities. Firstly, extrapolating the coexistence line between the two liquids at atmospheric pressure, the coexistence temperature would be $T \sim 3{,}700$ K: this would imply that the sp_3 liquid (and the glass) would be more stable than the sp_2 at room pressure up to very high temperatures, which is in contrast to the experimental data. Furthermore, J is proposed to have a linear dependence on T, so that, when $T \to 0$, also the mixing energy would tend to zero, i.e. at zero temperature the regular solution would become an ideal solution. This is extremely unusual.

Experimental Suggestions from the Graphite Melting Line Togaya [16] found a maximum in the melting line at $P_{max} = 5.6$ GPa. The author fitted the six experimental points with two straight lines: with positive slope at pressures lower than P_{max}, with negative slope at pressures higher than P_{max}. The discontinuous derivative of the melting curve at the maximum would imply there a triple point graphite/LDL/HDL, as a starting point of a LLPT coexistence line.

Prediction of a Short Range Bond Order Potential In Ref. [20] Glosli and Ree reported a complete study of a LLPT simulated with the Brenner bond order potential [35] in its version with torsional interactions [36]. The authors simulated in the canonical (NVT) ensemble several samples at increasing densities at eight different temperatures. By measuring the pressure, they show the familiar van der Waals loop denouncing mechanical instabilities at certain imposed densities. Using the Maxwell equal-area construction, the authors calculated the LLPT coexistence line, ending in a critical point at $T = 8{,}802$ K and $P = 10.56$ GPa. The lowest temperature coexistence point was calculated at $T = 5{,}500$ K and $P = 2.696$ GPa. The LDL/HDL coexistence line should meet the graphite melting line at its maximum, but unfortunately the BrennerI potential does not contain non bonded interactions, thus it cannot describe neither bulk graphite nor its melting line. To overcome this deficiency, the authors devised an ingenious perturbation method. Assuming constant slope of the negative sloped branch of the graphite melting line[6] and fixing the

[6] The authors adopted the graphite melting line measured by Togaya [16]. This melting line is reported in Fig. 1.4, together with our results. According to Glosli and Ree, from the maximum of that melting line would branch off the LLPT coexistence line.

graphite/diamond/HDL triple point at a value taken from the experimental literature, they give an estimate of the graphite/LDL/HDL triple point, at $T = 5{,}133\,\mathrm{K}$ and $P = 1.88$ GPa. The LDL was found to be mainly twofold (sp) coordinated with a polymeric-like structure, while the HDL was found to be a network forming, mainly fourfold, (sp_3) liquid. Following the predictions of this bond order potential, the sp_2 coordinated atoms would be completely avoided in the liquid. The authors identified the reason in the presence of torsional interactions. In fact, the increase in density demands an increase in structures with higher coordination than the sp, which is entropically favored at low densities. Each bonds of the sp_3 structures can freely evolve around the bond axis, while bonds between sp_2 sites are constrained in a (almost) planar geometry by the torsional interactions: this implies a low entropy for a liquid dominated by sp_2 sites. This low entropy would eventually destabilize the sp_2 sites towards the sp_3. To prove this conjecture, the authors calculated two relevant isotherms in the original version of the potential, without torsional interactions, finding no sign of a LLPT. Since some torsional interactions are definitely needed to mimic the double bond reluctancy to twist, the authors concluded that the LLPT predicted by the Brenner bond order potential with torsion is more realistic than its absence when torsional interactions are switched off.

Tight binding calculations [54] showed no evidence of van der Waals loops at some of the temperatures analyzed in Ref. [20]. As Glosli and Ree note, the tight binding model used in [54] is strictly two-center, thus the torsional interactions *cannot* be described.

An Ab Initio Confutation of the LLPT In Ref. [22], Wu et al. reported on a series of NVT-CPMD simulations at 6,000 K from density $1.27 - 3.02 \times 10^3$ kg/m^3, in a range where the BrennerI potential showed the first order LLPT at the same T. No sign of a van der Waals loop was found: in contrast to the BrennerI results of the previous section, two approaching series starting from the lowest and the highest density, were found to meet smoothly at intermediate densities. Looking for the reasons of the failure of the BrennerI potential, the authors calculated, with the same density functional (DF) used in the CPMD simulations, the torsional energy of two model molecules. One, $(CH_3)_2CC(CH_3)_2$ (see Fig. 2 in Ref. [30] for a schematic representation), was chosen so that the bond between the two central atoms represents a double bond in a carbon network: two sp_2 sites are bonded each to two sp_3 sites; the peripheral hydrogens are needed to saturated the sp_3 atoms and are intended to have no effect on the central bond. The second molecule, $(CH_2)_2CC(CH_2)_2$ (see again Fig. 2 in Ref. [30] for a schematic representation) is a portion of a completely sp_2 coordinated network: in the bond order language, the central bond is conjugated. The two molecules were geometrically optimized in their planar configurations and then twisted around the central bond axis in steps of $\pi/12$. In each configuration the electronic wave function was optimized, without further relaxations, to give the total energy, that was compared to the planar configuration total energy. The difference is the torsional energy. The DF calculations found a surprising picture (see Section 6.7 in Ref. [40] or Fig. 3 in Ref. [30]): while the double bond torsional energy was only slightly overestimated by the BrennerI potential